Network-Level Control of Frequency Tuning in Auditory Cortex

Hiroyuki K. Kato[1,2,*], **Samuel K. Asinof**[1], and **Jeffry S. Isaacson**[1,3,*]

[1]Center for Neural Circuits and Behavior and Department of Neurosciences, University of California, San Diego, La Jolla, CA, USA

SUMMARY

Lateral inhibition is a fundamental circuit operation that sharpens the tuning properties of cortical neurons. This operation is classically attributed to an increase in GABAergic synaptic input triggered by non-preferred stimuli. Here we use *in vivo* whole-cell recording and two-photon Ca^{2+} imaging in awake mice to show that lateral inhibition shapes frequency tuning in primary auditory cortex via an unconventional mechanism: non-preferred tones suppress both excitatory and inhibitory synaptic inputs onto layer 2/3 cells ("network suppression"). Moreover, optogenetic inactivation of inhibitory interneurons elicits a paradoxical increase in inhibitory synaptic input. These results indicate that GABAergic interneurons regulate cortical activity indirectly via the suppression of recurrent excitation. Furthermore, the network suppression underlying lateral inhibition was blocked by inactivation of somatostatin-expressing interneurons (SOM cells), but not parvalbumin-expressing interneurons (PV cells). Together, these findings reveal that SOM cells govern lateral inhibition and control cortical frequency tuning through the regulation of reverberating recurrent circuits.

In Brief

Kato et al. show that lateral inhibition shapes frequency tuning in primary auditory cortex via an unconventional mechanism: non-preferred stimuli suppress recurrent excitation. Somatostatin-expressing interneurons are critical for triggering this indirect form of cortical inhibition.

INTRODUCTION

In sensory cortical areas, neurons sharply tuned to particular features of sensory stimuli underlie precise representations of the external world. For example, pyramidal cells in visual cortex respond selectively to visual stimuli with a certain orientation or size, those in rodent somatosensory cortex prefer particular directions of whisker deflection, and neurons in auditory cortex fire selectively to certain sound frequencies. Revealing the factors governing

cortical tuning properties is fundamental for understanding how sensory information is encoded in the brain.

The excitatory synaptic input driving tuned pyramidal cell activity comes from two main sources: afferent thalamic inputs and recurrent synapses between pyramidal cells themselves that amplify thalamic input (Li et al., 2013; Lien and Scanziani, 2013). While excitation broadly defines the tuning of pyramidal cell spike output, stimulus selectivity can be further refined by inhibitory synaptic input (Isaacson and Scanziani, 2011; Priebe and Ferster, 2008). Cortical inhibition is mediated by a variety of local GABAergic interneurons that are highly interconnected with pyramidal cells as well as each other (Pfeffer et al., 2013; Tremblay et al., 2016). However, the precise synaptic mechanisms by which interconnected excitatory and inhibitory circuits generate pyramidal cell tuning properties are not established.

Lateral inhibition, first described in photoreceptors (Hartline et al., 1956), is a basic circuit operation that can sharpen cortical tuning properties (Isaacson and Scanziani, 2011; Priebe and Ferster, 2008). In this operation, pyramidal cells firing in response to stimuli in their receptive fields recruit local interneurons, which in turn suppress firing of other neurons with different receptive fields. In a classical model, lateral inhibition narrows tuning of individual neurons when non-preferred stimuli recruit inhibitory synaptic input more strongly than excitation. In other words, lateral inhibition occurs when synaptic inhibition is more broadly tuned than excitation. Indeed, differences in the tuning broadness of excitation and inhibition have been proposed to enforce odor selectivity in olfactory cortex (Poo and Isaacson, 2009) as well as selectivity for the size (Adesnik et al., 2012) and orientation (Liu et al., 2011; but see Tan et al., 2011) of visual stimuli in visual cortex.

Interestingly, in primary auditory cortex the extent to which lateral inhibition contributes to frequency tuning as well as the synaptic mechanisms underlying suppressive effects of non-preferred stimuli are a matter of debate. For example, studies in primates, cats, and rodents using two-tone protocols have found that firing to preferred frequencies can be suppressed when preceded by tones that are octaves different (Calford and Semple, 1995; Li et al., 2014; Phillips and Cynader, 1985; Sadagopan and Wang, 2010; Sutter et al., 1999). Although two-tone suppression is typically attributed to GABAergic inhibition produced by the first sound, synaptic depression of excitatory input has also been shown to contribute to suppressed activity in this paradigm (Wehr and Zador, 2005). More typical of classic lateral inhibition, single tones at non-preferred frequencies have also been found to cause suppression of spontaneous neuronal firing in awake primates (O'Connell et al., 2011; Sadagopan and Wang, 2010). However, these reports of response suppression are difficult to reconcile with intracellular recordings of sound-evoked synaptic responses in rodent auditory cortex. For instance, studies have found completely balanced excitation and inhibition in layer 2/3 (L2/3) and layer 4 (Wehr and Zador, 2003; Zhang et al., 2003; Zhou et al., 2014) or inhibition tuned only slightly broader than excitation (Li et al., 2014; Wu et al., 2008). In this "co-tuning" scenario, inhibition would contribute to frequency tuning by ensuring that only the strongest excitatory input depolarizes cells to spike threshold, a mechanism known as the "iceberg effect" (Carandini and Ferster, 2000). Since this effect

regulates tuning only in a rather narrow range around the preferred frequency, the synaptic mechanisms underlying broad side-band suppression remain unknown.

Here, we use *in vivo* two-photon calcium imaging and whole-cell recordings to show pronounced lateral inhibition in primary auditory cortex (A1) of awake mice. In individual neurons, firing could be suppressed by tones octaves away from their preferred frequencies, arguing against a simple "iceberg" model of lateral inhibition. Indeed, we find that lateral inhibition shapes frequency tuning via an unconventional mechanism: non-preferred sounds do not increase inhibitory inputs onto individual neurons, but rather suppress both excitatory and inhibitory inputs (network suppression). Furthermore, we demonstrate that the inactivation of SOM interneurons, but not PV interneurons, blocks the network suppression evoked by non-preferred sounds. Taken together, our findings are most consistent with the idea that lateral inhibition is mediated by SOM cells, which regulate cortical tuning via the indirect regulation of ongoing recurrent excitation in the cortical network.

RESULTS

We first investigated lateral inhibition in A1 by testing the frequency tuning properties of a large population of L2/3 pyramidal cells using two-photon calcium imaging in awake head-fixed mice (Figure 1A). To isolate action potential-dependent responses of excitatory pyramidal cells, the Ca^{2+} indicator GCaMP6s was expressed in mice in which GABAergic inhibitory neurons were marked with tdTomato (*Gad2-IRES-Cre × ROSA-LSL-tdTomato* mice). Tonal receptive fields (TRFs) of individual L2/3 pyramidal cells were measured by presenting pure tones (1 s) across a range of frequencies (2–40 kHz) and intensities (30–70 dB). On average, 41.7% ± 8.1% of GCaMP6s-expressing pyramidal cells (n = 1,681 cells, 8 mice) increased their activity (measured as dF/F) in response to at least one frequency, and many of those cells (41.3%) displayed classical "V-shaped" TRFs (Figure 1B, top; Figure S1). A similar fraction of pyramidal cells (32.3% ± 7.2%) decreased their activity in response to at least one frequency, as previously reported in awake mice (Kato et al., 2015). Importantly, lateral inhibition was clearly present, since pyramidal cells could have both excitatory and suppressive responses to non-overlapping frequencies (Figure 1B, bottom). We determined average TRFs across all excited cells (n = 749) by centering tuning curves to their best frequencies (BF, frequency eliciting the strongest response regardless of intensity) for excitation. Interestingly, the population TRFs revealed prominent suppressive responses evoked by frequencies one to four octaves higher than the BF for excitation (Figure 1C). Though weaker in relative magnitude, suppressive responses were also apparent at frequencies one to four octaves lower than excitatory BF. The wide separation between excitatory and suppressive TRFs (Figures 1C and S1) we observe cannot arise from approximately balanced synaptic excitation and inhibition. Rather, our results indicate that lateral inhibition biased toward frequencies higher than those driving excitation shapes frequency tuning in A1 of awake mice.

To investigate how lateral inhibition could be biased toward the higher-frequency side of excitatory TRFs, we examined the spatial distribution of tuned excitatory or suppressive responses along the A1 tonotopic axis. Tonotopy was mapped with intrinsic signal imaging using pure tones of three frequencies (3, 10, and 30 kHz), and two-photon imaging fields of

view were registered to the intrinsic signal using the surface vasculature (Figure 1D). We determined the spatial organization for excitatory and suppressive tuning at the cellular level using activity maps representing the characteristic frequencies (CF, frequency with strongest response at lowest effective sound intensity) of responsive cells. As reported previously (Issa et al., 2014; Kato et al., 2015), we observed a cellular-level tonotopic organization of excitatory CFs that coarsely adhered to the tonotopic axis identified by macroscopic imaging (Figure 1D). In contrast, CFs for suppression lacked clear tonotopic organization and showed a relatively uniform distribution throughout the tonotopic axis. We quantified the tonotopic distribution of cells across mice by plotting the CFs of all responsive neurons against their positions along the normalized A1 tonotopic axis (3–30 kHz, Figure 1E; n = 8 mice, 443 cells with excitatory responses, 405 cells with suppressive responses). As expected, excitatory CFs increased monotonically from the low to high end of the tonotopic axis. In contrast, suppressive CFs were only weakly correlated with location along the tonotopic axis, and higher frequencies were overrepresented all across A1. Thus, the differential tuning of excitation and suppression along the tonotopic axis results in a bias for lateral inhibition toward the higher-frequency side of excitatory TRFs. Furthermore, the differential tuning of excitatory and inhibitory TRFs in individual neurons is in apparent contradiction with the idea of co-tuned synaptic excitation and inhibition in A1.

What mechanisms underlie lateral inhibition in A1 under our conditions? To address this question we used blind patch clamp recording to study sound-evoked responses of L2/3 cells in awake mice. In current clamp recordings (resting potential -62 ± 2 mV, n = 12), cells had regular action potential firing with spike widths typical of pyramidal cells (Figure 2A; 1.22 $\pm$ 0.07 ms, n = 8 cells). In addition, spikes recorded in cell-attached mode for 30/31 blind whole-cell recordings in this study had waveforms distinct from fast-spiking (FS) interneurons (Figure S2). Given that pyramidal cells make up the bulk of non-FS cells in L2/3, we refer to the recorded neurons in this study as "pyramidal cells." Tones (100–200 ms duration) evoked membrane depolarization at particular (preferred) frequencies and this excitation became progressively briefer before switching to pure hyperpolarizing responses as frequencies shifted away from the preferred stimulus (Figures 2A and 2B; peak hyperpolarization 8.8 $\pm$ 0.9 mV, n = 10 cells). Consistent with our imaging results, suppressive responses to non-preferred tones abolished action potentials when membrane potential was moved above spike threshold with depolarizing current injection (Figure 2B; 95% $\pm$ 3% suppression, n = 6 cells, p = 2×10^{-3}). Intriguingly, we found that cell input resistance increased significantly (p = 0.03) during the hyperpolarization evoked by non-preferred frequencies (Figure 2C). This is puzzling since synaptic inhibition classically requires activation of a GABAergic synaptic conductance that lowers membrane resistance (Isaacson and Scanziani, 2011). Indeed, this finding indicates that an unconventional synaptic mechanism underlies lateral inhibition in auditory cortex.

We next used voltage-clamp recording to directly determine the postsynaptic currents that shape frequency tuning in A1. Excitatory postsynaptic currents (EPSCs) and inhibitory postsynaptic currents (IPSCs) were recorded near the reversal potentials for synaptic inhibition and excitation, respectively (Figure S3). Recordings in awake mice revealed sustained, high-frequency barrages of spontaneous EPSCs and IPSCs, indicating that cortical circuits were highly active even in the absence of delivered tones (Figure 3A). In

contrast, we observed relatively low basal activity interrupted by irregular bursts of synaptic activity if the pipette internal solution included the voltage-gated sodium channel blocker QX-314 (5 mM, Figure S4) or if the cortex was damaged due to poor surgical exposure of the brain surface or excessive pipette penetrations (STAR Methods). Remarkably, under our conditions of high cortical activity, presentation of non-preferred tones suppressed both spontaneous EPSCs and IPSCs (Figures 3A and 3B; reduction in variance, EPSC, 26.5% ± 3.8%; IPSC, 35.5% ± 5.8%). This suppression of ongoing network activity ("network suppression") by non-preferred stimuli is completely different from the selective increase in IPSCs expected for classical lateral inhibition. Rather, these results indicate that the membrane hyperpolarization underlying lateral inhibition in A1 is due to the withdrawal of excitatory synaptic input, which is likely driven indirectly by local interneurons.

Our results raise the possibility that preferred and non-preferred stimuli trigger distinct inhibitory circuit operations. We tested this by measuring the frequency tuning of excitatory and inhibitory synaptic currents. Indeed, averaged responses (five to ten trials per frequency-intensity pair, 100 ms tone duration) from individual neurons displayed two types of synaptic activity that differed in their kinetics and tuning (Figures 4A, 4B, and S5). We observed transient, sound onset-locked EPSCs ($EPSC_{ON}$) and IPSCs ($IPSC_{ON}$) with overlapping TRFs similar to previous reports in A1 (Li et al., 2014; Wehr and Zador, 2003; Wu et al., 2008; Zhang et al., 2003; Zhou et al., 2014). However, higher-frequency tones evoked a slow suppression of spontaneous EPSCs and IPSCs, which on average traces appear as slow currents opposite in polarity to onset-locked responses. Interestingly, while sustained suppression of synaptic activity was also observed with longer duration (1 s) tones, brief 15 ms tone "pips" evoked predominantly transient, sound onset-locked responses (Figure S5). The slow components do not reflect voltage-clamp errors that reverse $IPSC_{ON}$ and $EPSC_{ON}$ since the kinetics and tuning of the fast and slow currents are distinct, nor do the slow components require activation of presynaptic $GABA_B$ receptors (Urban-Ciecko et al., 2015) (Figure S6). They also do not reflect shunting inhibition, since non-preferred stimuli increase input resistance (Figure 2C). Rather, we consider these slow components, $EPSC_{NS}$ and $IPSC_{NS}$, to be due to the withdrawal of spontaneous synaptic activity during network suppression.

The TRFs of $EPSC_{ON}$ and $IPSC_{ON}$ largely overlap (Figures 4C and 4D), with $IPSC_{ON}$ more broadly tuned, consistent with previous findings in L2/3 (Li et al., 2014; but see Zhou et al., 2014). However, the difference in tuning broadness (half-maximal bandwidth) is only 0.4 octaves and cannot account for the suppression of spike output one to four octaves from best frequency (Figure 1C). Thus, a conventional model for lateral inhibition solely based on broadly tuned inhibitory synaptic input does not apply to frequency tuning in A1 of awake mice. In contrast, the tuning of $EPSC_{NS}$ and $IPSC_{NS}$ is shifted far from $EPSC_{ON}$ best frequency (distance to peak $EPSC_{NS}$ and $IPSC_{NS}$: 1.4 ± 0.2 octaves and 1.6 ± 0.1 octaves, respectively) and covers the range of frequencies for lateral inhibition observed with GCaMP6s imaging. Taken together, these results suggest that the frequency tuning properties of L2/3 cells are regulated by inhibitory neurons acting via both direct synaptic inputs (preferred tones) and indirect decreases in network activity (non-preferred tones).

What cortical regime can produce lateral inhibition via a decrease in excitatory synaptic input? We considered the idea that the cortex might operate as an inhibition-stabilized network (ISN), a proposed model in which recurrent excitation is strong enough to destabilize the cortical network unless it is tightly regulated by recurrent inhibition (Litwin-Kumar et al., 2016; Ozeki et al., 2009; Rubin et al., 2015; Tsodyks et al., 1997). In ISNs, lateral input onto inhibitory interneurons transiently increases inhibition and suppresses excitatory neurons. However, since strong recurrent excitation tightly regulates interneuron firing, a new steady state is reached in which both excitatory and inhibitory neuron activities are reduced. Although this regime has been suggested for cortical processing (Litwin-Kumar et al., 2016; Ozeki et al., 2009; Rubin et al., 2015; Sato et al., 2016; Tsodyks et al., 1997), proof of ISN operation has not been well established.

To directly determine whether A1 acts as an ISN, we tested a central hypothesis of this network model: suppression of inhibitory neurons should cause a transient reduction of inhibitory input onto individual pyramidal cells, followed by a paradoxical increase in synaptic inhibition (Litwin-Kumar et al., 2016; Ozeki et al., 2009; Tsodyks et al., 1997). The majority of cortical inhibition is mediated by SOM-, PV-, and vasoactive intestinal peptide (VIP)-expressing interneurons (Pfeffer et al., 2013; Rudy et al., 2011; Xu et al., 2010). As a population, cortical VIP cells only weakly inhibit pyramidal cells (Pfeffer et al., 2013) and we found that tones largely produced inhibition of VIP cells (Figure S1). Thus, we focused attention on SOM and PV cells which provide the major sources of inhibition onto pyramidal cells. We recorded EPSCs and IPSCs in L2/3 and photoinactivated SOM (Figure 5A) or PV cells (Figure 5B), using the hyperpolarizing opsin halorhodopsin (eNpHR3). We used weak LED intensities to modulate transmission without inducing aberrant discharges (STAR Methods). Exactly as predicted for an ISN, photoinactivation of SOM or PV cells produced a transient reduction in tonic inhibitory currents followed by a sustained increase in IPSCs (Figures 5A and 5B; IPSC amplitude, PV = 137 ± 33 pA, p = 0.002; SOM = 61 ± 23 pA, p = 0.02, 100–200 ms following LED onset). As expected, EPSCs showed a monotonic enhancement coinciding with the IPSC increase (EPSC amplitude, PV = -88 ± 19 pA, p = 0.001; SOM = -73 ± 18 pA, p < 0.001). These results strongly support the idea that auditory cortex operates as an ISN in awake animals and reveal the foundation for the reduced excitation during lateral inhibition.

Which class of interneurons is responsible for regulating cortical network activity during lateral inhibition? To address this question, we tested how SOM and PV cell inactivation affected tone-evoked synaptic responses. Remarkably, levels of SOM cell photoinactivation with little effect on sound onset-locked direct responses significantly reduced slow, indirect responses to non-preferred tones (Figures 6A and 6B; $EPSC_{NS}$ charge, p = 0.002; $IPSC_{NS}$ charge, p = 0.011; n = 7 cells, 5 mice). This shows that SOM cells provide inhibition critical for triggering network suppression. In contrast, PV cell photoinactivation that had little effect on direct responses significantly enhanced network suppression of EPSCs. The effect on network suppression of IPSCs was more variable, but had a tendency for enhancement (Figures 6C and 6D, $EPSC_{NS}$, p = 0.004; $IPSC_{NS}$, p = 0.066, n = 8 cells, 5 mice). The simplest explanation for this result is that PV cells do not underlie network suppression by non-preferred tones. Rather, PV cell inactivation increases the amount of spontaneous synaptic activity that SOM cells can suppress. Taken together, the bidirectional effects of

these local interneuron populations rule out the possibility that network suppression is simply inherited from subcortical systems and reveal a necessary role for cortical SOM cells in lateral inhibition.

What mechanisms enable SOM cells to mediate lateral interactions across cortical frequency domains? One possibility is that SOM cells are untuned (or anti-tuned) and provide broad inhibition onto local A1 pyramidal cells. We tested this by imaging GCaMP6s-expressing SOM and PV cells (Figure 7) and comparing their frequency tuning relative to pyramidal cells (Figure 1). Interestingly, like pyramidal cells, CFs for excitation of both SOM and PV cells had cellular-level tonotopic organization coherent to the global tonotopic axis identified by macroscopic imaging (Figures 7A–7E), arguing against the notion that SOM cells are uniquely untuned. Another possibility is that SOM cell tuning might be "broad enough" to underlie lateral inhibition. Indeed, in contrast to results in anaesthetized mice (Li et al., 2014, 2015), we found that SOM cells were more broadly tuned than pyramidal or PV cells (Figures 7C, 7F, and S1). Furthermore, while PV cells showed similar tuning to pyramidal cells (Moore and Wehr, 2013), including lateral inhibition, SOM cells were rarely inhibited. The distinct sound evoked responses of SOM and PV cells cannot be explained by differences in spontaneous activity since targeted loose patch recordings of SOM and PV cells (Figure S2) revealed similar rates of spontaneous action potentials (PV cells = 4.3 ± 1.2 Hz, n = 10; SOM cells = 3.6 ± 1.3 Hz, n = 12, p = 0.34). Broadly tuned SOM cell excitation in A1 is consistent with the high convergence of horizontal excitatory input onto SOM cells in visual cortex proposed to underlie surround suppression (Adesnik et al., 2012). However, the tuning bandwidth of SOM cells (2.1 ± 0.1 octaves at 70 dB) alone does not appear broad enough to account for the lateral inhibition found two to four octaves from the preferred frequency of pyramidal cells.

We next considered whether the horizontal range of SOM cell-mediated inhibition could contribute to distant lateral interactions in A1. To test this, we used focal (60 μm diameter) photoactivation at sites along the A1 tonotopic axis in slices from mice expressing channelrhodopsin-2 (ChR2) selectively in SOM or PV cells (Figure 8A). Recordings were performed in the presence of glutamate and $GABA_B$ receptor blockers and ramp illumination (470 nm, 0.2–2 s) was used to activate somatodendritic compartments of PV and SOM cells within the photostimulated area rather than ChR2-expressing axons (Adesnik and Scanziani, 2010). We saw no difference in recordings from the low versus high-frequency regions of slices (data not shown), and results using either direction of stimulation along the tonotopic axis were pooled. L2/3 pyramidal cell IPSCs elicited by PV cell activation diminished rapidly as the photostimulus was moved laterally from the recorded cell (Figure 8B). In contrast, SOM cell-evoked inhibition was sustained over a greater distance (average length constant PV cells, 129 μm; SOM cells, 295 μm). Photostimulation along cortical columns (Figure 8C) revealed that SOM cells also provide more diffuse translaminar inhibition than PV cells (Figure 8D). Taken together, we propose that SOM cells mediate lateral interactions between distant A1 frequency domains through both the convergence of excitatory inputs and divergence of inhibitory outputs across horizontal cortical space.

DISCUSSION

Lateral Inhibition in the Primary Auditory Cortex

In A1 of awake mice, ensemble imaging of L2/3 pyramidal cells reveals divergent receptive fields for tone frequencies that increase and suppress firing activity. Although previous unit recording studies in anesthetized animals did not describe suppressive TRFs using single tones (Calford and Semple, 1995; Li et al., 2014; Phillips and Cynader, 1985; Sutter et al., 1999), this is likely because anesthesia results in low levels of spontaneous activity that preclude measurement of firing suppression. Consistent with this idea, studies in awake animals report that single tones suppress spontaneous firing and suppressive TRFs extend octaves away from the neuron's best frequency (Kato et al., 2015; O'Connell et al., 2011; Pelleg-Toiba and Wollberg, 1989; Sadagopan and Wang, 2010; Shamma and Symmes, 1985). Interestingly, the lateral inhibition of firing activity under our conditions shows a strong bias to the high-frequency side of excitatory TRFs. A similar bias has been reported for the frequency tuning of on and off responses in auditory cortex, with off responses tuned one to two octaves above on responses (Scholl et al., 2010). However, network suppression is not an off response, since it develops well before sound offset and has an opposite polarity. The bias we describe could result from the differential tuning of excitation and suppression we find along the 2–40 kHz tonotopic axis of A1; whereas the excitatory CFs of individual neurons matched their location along the macroscopic tonotopic axis, suppressive CFs showed a relatively uniform overrepresentation of higher frequencies all along A1. This position-invariant distribution of suppressive CFs supports the idea that the tuning of inhibition is not determined by local activity, but rather by pooling activity across wide areas of A1. However, our results do not exclude the possibility that cells in other areas representing higher ultrasonic frequencies have suppressive TRFs biased to the low-frequency side of excitatory TRFs.

We used whole-cell recording in awake mice to reveal the synaptic mechanisms underlying lateral inhibition. Consistent with our imaging results, current clamp recordings revealed that non-preferred frequencies evoke strong membrane hyperpolarization sufficient to abolish pyramidal cell spike firing. The fact that hyperpolarization was elicited by frequencies octaves away from the best frequency for depolarization appears to contradict studies that used voltage clamp to isolate tone-evoked synaptic excitation and inhibition (Li et al., 2014; Tan and Wehr, 2009; Wehr and Zador, 2003; Wu et al., 2008; Zhang et al., 2003; Zhou et al., 2014). Although these studies include cells in multiple layers and vary with respect to the absolute tuning broadness reported for inhibition, they all come to the conclusion that tuning curves for synaptic excitation and inhibition are largely overlapping. Importantly, using voltage-clamp recording, we show that this discrepancy can be explained by the presence of two different components underlying sound-evoked responses in A1. First, consistent with previous reports, we show that tones evoke sound onset-locked synaptic responses and that evoked IPSCs are tuned to a slightly broader range of frequencies than those that evoke EPSCs. However, the TRFs for these conventional sound-evoked IPSCs cannot account for suppression of firing activity that is octaves away from a neuron's best frequency. Instead, we demonstrate that this lateral inhibition is caused by a second, previously undocumented component of sound-evoked responses: the suppression of

both excitatory and inhibitory synaptic inputs. The suppression of spontaneous activity has a longer latency and slower time course than onset-locked increases in synaptic activity. More importantly, the TRF of sound-evoked network suppression diverges from the tuning of onset-locked inputs and covers a frequency range that can be octaves away from the preferred frequency for onset-locked responses.

The network suppression we report provides a synaptic mechanism for broad lateral inhibition of firing activity. Interestingly, in unit recordings, the kinetics of two-tone suppression of neuronal firing differ between frequency domains that are proximal or distal to the neuron's preferred frequency (Sadagopan and Wang, 2010; Sutter and Loftus, 2003). One possibility is that "lateral inhibition" actually consists of multiple distinct mechanisms: in the frequency domain around the excitatory synaptic TRF, a slightly broader TRF for sound onset-locked inhibition sharpens neuronal firing via the iceberg effect. In contrast, in the frequency domain distal to the preferred frequency, lateral inhibition is enabled by the slow network suppression of ongoing recurrent synaptic activity. In primates, suppression observed at the population level has also been attributed to a combination of feedforward inhibition and a phase reset of ongoing cortical oscillations (O'Connell et al., 2011). It is likely that multiple mechanisms work together to shape cortical dynamics and generate lateral inhibition in the awake brain.

Why have prior *in vivo* whole-cell recording studies not reported the slow network suppression we observe in the majority of recorded neurons? We found that brief (15 ms) tone pips elicit very weak network suppression, thus it may simply have been missed in previous studies that did not use stimuli of sufficient duration. We think the use of anesthetics in most previous studies is also a major factor. Anesthesia dampens activity in many neural circuits, and spontaneous activity of A1 neurons is much higher in awake animals (Gao et al., 2016; Kato et al., 2015). Indeed, the continuous high-frequency barrages of spontaneous excitatory and inhibitory inputs we observe differ from the generally "quiet" baseline activity observed in previous studies using *in vivo* voltage-clamp recording. However, even in our recordings in awake animals, we observed conditions that compromised cortical activity. Low levels of spontaneous activity and TRFs lacking slow network suppression were observed when the pipette internal solution contained QX-314, an intracellular blocker of voltage-gated Na^+ and Ca^{2+} channels (Strichartz, 1973; Talbot and Sayer, 1996) often used in millimolar concentrations for recordings of synaptic transmission (Li et al., 2014; Scholl et al., 2010; Wehr and Zador, 2003; Zhou et al., 2014). However, micromolar QX-314 blocks action potentials in a use-dependent manner when applied extracellularly (Hessler et al., 1993). Given the positive pipette pressure used when searching for cells with blind whole-cell recording, spill of QX-314 should cause a long-lasting reduction in network activity. Thus, factors such as stimulus duration, anesthesia, QX-314 pipette solutions, and cortical damage could have resulted in low spontaneous cortical activity in prior studies, and likely precluded the detection of network suppression. Regardless of the reasons for the difference, our intracellular results can entirely account for the lateral inhibition of firing activity we observed. Thus, we believe network suppression is likely to be a physiological phenomenon that shapes frequency tuning in the auditory cortex of awake animals.

Inhibitory Neuron Circuits in the Primary Auditory Cortex

We demonstrate that SOM cells, but not PV cells, are critical for the triggering of network suppression by non-preferred stimuli. This result suggests that SOM cells mediate lateral inhibition by linking spatially distant frequency domains of A1. Indeed, we show that SOM cells are the most broadly frequency tuned cells in L2/3, suggesting a convergence of frequency information from wide A1 areas onto individual SOM cells. In contrast, PV cells are only slightly more broadly tuned than pyramidal cells. This is consistent with a previous study reporting the similar frequency tuning of PV and pyramidal cells in A1 (Moore and Wehr, 2013). These results suggest that PV cell activity arises from information sampled from local pyramidal cells. Although another study in A1 of anesthetized animals suggested that PV cells are more broadly tuned than SOM or pyramidal cells (Li et al., 2015), this may be due to the fact that anesthesia strongly attenuates SOM cell activity (Adesnik et al., 2012). Similar to our findings in A1, SOM cells in primary visual cortex are reported to integrate horizontal inputs across wide regions of cortical space, and this convergence underlies surround suppression across retinotopic domains (Adesnik et al., 2012). Therefore, lateral inhibition mediated by broadly tuned SOM cells is likely to be a general mechanism across sensory cortices.

In our study, the tuning broadness of SOM cells in A1 (bandwidth at 70 dB, 2.1 ± 0.1 octaves) is not enough to fully account for the lateral inhibition that covers up to three to four octaves away from an individual neuron's preferred frequency. This suggests the presence of an additional mechanism by which SOM cells regulate lateral interactions. Indeed, using focal photoactivation of interneurons along the A1 tonotopic axis, we demonstrate that SOM cell-mediated inhibition extends over 500 μm, which corresponds to over two octaves along the A1 tonotopic axis (determined from intrinsic imaging). This broad inhibitory output range gives SOM cells an additional ability to link laterally distributed cortical areas. Curiously, the inhibitory range observed in our study is double the distance reported by a previous study (Li et al., 2014). This difference is possibly attributed to our use of a slow ramping photostimulus which is more effective in firing action potentials from intact cells than bypassing axons (Adesnik and Scanziani, 2010). Alternatively, the difference could be explained by our use of cortical slices maintaining the A1 tonotopic axis. Taken together, our results demonstrate that lateral inhibition in A1 is mediated by both the convergence of inputs onto SOM cells and divergence of outputs from SOM cells. These results suggest that SOM cells work as a hub for the lateral flow of information in cortical circuits, and regulate the integration of information across spatially distributed auditory frequency domains.

Operating Regime of Inhibition in Cortical Networks

In highly interconnected cortical circuits, activity of one neuron affects others not just via direct synaptic input, but also via a cascade of indirect network-level effects. The suppression of both excitatory and inhibitory inputs by non-preferred tones indicates that SOM cells trigger lateral inhibition not through direct inhibitory input onto pyramidal cells, but rather through a suppression of recurrent excitation in the A1 network. This result is consistent with the operation of A1 as an ISN, a network model where strong recurrent excitation in the circuit is constantly regulated by inhibition to prevent run-away activity

(Litwin-Kumar et al., 2016; Ozeki et al., 2009; Rubin et al., 2015; Tsodyks et al., 1997). Our observation of a paradoxical increase in IPSCs during optogenetic inactivation of inhibitory neurons further supports this model (Tsodyks et al., 1997). We note that simultaneous suppression of both excitation and inhibition could also be explained by another mechanism. For example, SOM cells could suppress pyramidal cell activity via silent, shunting inhibition while at the same time inhibiting PV cells that provide the majority of conventional pyramidal cell IPSCs. However, this model fails to explain the paradoxical increase in inhibitory inputs during optogenetic inactivation of PV cells, and therefore the most parsimonious explanation is that A1 in awake brain operates as an ISN. Nevertheless, our results do not exclude the possibility that both mechanisms contribute to the ability of SOM cells to mediate network suppression during lateral inhibition.

Whether or not cortical circuits operate in a regime of strong recurrent excitation and indirect effects of inhibitory interneurons is a subject of debate. In visual cortex, while results consistent with ISN behavior have been observed (Ozeki et al., 2009; Sato et al., 2016), other studies are more consistent with weak recurrent excitation and direct inhibition of pyramidal cells (Adesnik et al., 2012; Atallah et al., 2012; Haider et al., 2010, 2013). It is plausible that, in the anesthetized state, where most neurons are sitting far below firing threshold, sensory stimuli fail to recruit recurrent excitation. In the awake state, in contrast, since neurons are already close to firing threshold even without sensory stimuli (Constantinople and Bruno, 2011; Reinhold et al., 2015; Steriade et al., 2001), sensory inputs can recruit strong recurrent excitation from horizontally connected neurons such that the cortical circuits operate as an ISN. One intriguing possibility is that those two circuit operation regimes are not mutually exclusive, but rather form a continuous spectrum of operation modes that is determined by the level of arousal (McGinley et al., 2015). In future, it would be of interest to investigate how lateral inhibition is affected by various brain states associated with arousal, attention (Zhang et al., 2014) or behavior (Kato et al., 2015; Schneider et al., 2014).

Implications for Auditory Processing in A1 Circuits

The unique spectro-temporal features of network suppression provide A1 neurons an expanded capacity for auditory processing. One aspect that distinctly differentiates network suppression from sound onset-locked inhibition is its shifted tuning. We find that network suppression in individual cells can be evoked by frequencies as high as four octaves away from the neurons' preferred frequency. This extended domain of inhibition not only sharpens the frequency tuning of individual A1 neurons against single tones, but it could also provide neurons with a spectral filter against sound stimuli with multiple frequencies. For example, presentation of high-frequency target sounds could trigger network suppression throughout the entire A1 tonotopic axis and thus filter out broadband background noise to enhance the saliency of the target. This idea is of special interest, considering the bias of network suppression toward high frequencies (20–40 kHz). Mice use high-frequency ultrasonic vocalizations to communicate with each other, and behaviorally are most sensitive to frequencies in this range (Mikaelian et al., 1974). This strong sensitivity to ultrasonic frequencies may be further enhanced by lateral inhibition that extends from the high-frequency to low-frequency domain of A1. It is possible that the mouse auditory system is

organized to suppress responses to low-frequency sounds in the presence of high-frequency sounds, such that behaviorally relevant ultrasonic vocalizations are preferentially processed to guide behavior.

Another important aspect that differentiates network suppression from sound onset-locked inhibition is its prolonged duration. In contrast to transient sound onset-locked inhibition that usually lasts for less than 50 ms (Wehr and Zador, 2003, 2005; Zhang et al., 2003; Zhou et al., 2014), network suppression lasts considerably longer. This prolonged suppression allows individual A1 neurons to integrate information over longer time periods. For example, we find that prolonged network suppression can follow transient excitatory synaptic responses even at the preferred frequencies of neurons (Figure 4B). It may be the case that slow network suppression contributes to forward suppression (masking), where a preferred frequency tone can suppress responses to a subsequent tone delivered hundreds of milliseconds later (Wehr and Zador, 2005). Ultimately, through the recruitment of reverberating recurrent circuits, network suppression expands the capacity for cortical integration along both the spatial and temporal domains.

STAR★METHODS

KEY RESOURCES TABLE

REAGENT or RESOURCE	SOURCE	IDENTIFIER
Bacterial and Virus Strains		
AAV2/9.syn.GCaMP6s.WPRE.SV40	Penn Vector Core	AV-9-PV2824
AAV2/9.syn.FLEX.GCaMP6s.WPRE.SV40	Penn Vector Core	AV-9-PV2821
AAV2/9.EF1a.DIO.hChR2(H134R).EYFP.WPRE.hGH	Penn Vector Core	AV-9-20298P
AAV2/9.CBA.FLEX.hChR2(H134R).mCherry.WPRE.SV40	Penn Vector Core	AV-9-18916P
AAV2/9.EF1a.DIO.eNpHR3.0.EYFP.WPRE.hGH	Penn Vector Core	AV-9-26966P
Chemicals, Peptides, and Recombinant Proteins		
NBQX	Tocris	Cat. 1044, CAS 479347-86-9
CGP 55845	Tocris	Cat. 1248, CAS 149184-22-5
Experimental Models: Organisms/Strains		
$Gad2^{tm2(cre)Zjh}$/J (Gad2-cre)	The Jackson Laboratory	010802
B6;129P2-$Pvalb^{tm1(cre)Arbr}$/J (PV-cre)	The Jackson Laboratory	008069
$Sst^{tm2.1(cre)Zjh}$/J (SOM-cre)	The Jackson Laboratory	013044
$Vip^{tm1(cre)Zjh}$/J (VIP-cre)	The Jackson Laboratory	010908
B6.Cg-$Gt(ROSA)26Sor^{tm32(CAG-COP4*H134R/EYFP)Hze}$/J (Ai32)	The Jackson Laboratory	024109
B6;129S6-$Gt(ROSA)26Sor^{tm14(CAG-tdTomato)Hze}$/J (Ai14)	The Jackson Laboratory	007908
Software and Algorithms		
MATLAB (versions 2012b, 2014b)	MathWorks	RRID:SCR_001622
ScanImage (version 4.2)	Vidrio Technologies	RRID:SCR_014307
AxoGraph X	Axograph	RRID:SCR_014284
BControl	Carlos Brody, Princeton	http://brodylab.org

REAGENT or RESOURCE	SOURCE	IDENTIFIER
Other		
Bscope (2-photon resonant microscope)	ThorLabs	(N/A)
Multiclamp 700 amplifier	Molecular Devices	https://www.moleculardevices.com
Electrostatic speaker (ES-1)	Tucker Davis Technologies	https://www.tdt.com
CCD-1300QF Camera	VDS Vosskühler	(N/A)
MP-285 Manipulator	Sutter Instruments	https://www.sutter.com
Digitizer (ITC-18)	HEKA	https://www.heka.com

CONTACT FOR REAGENT AND RESOURCE SHARING

Further information and requests for resources and reagents should be directed to and will be fulfilled by the Lead Contact, Jeffry Isaacson (jisaacson@ucsd.edu).

EXPERIMENTAL MODEL AND SUBJECT DETAILS

Mice between 6 and 10 weeks of age were used for all experiments. Mice were acquired from Jackson Laboratories (*GAD2 –Cre, PV-Cre, SOM -Cre, VIP-Cre, Rosa-LSL-ChR2(H134R)-EYFP*, and *Rosa-LSL-tdTomato*). Both female and male animals were used and maintained on a 12:12 reversed light:dark cycle. Experiments were performed during the dark period. Mice had no prior history of experimental procedures that could affect the results. All procedures were in accordance with protocols approved by the UCSD Institutional Animal Care and Use Committee and guidelines of the National Institute of Health.

METHOD DETAILS

Preparation for In Vivo Two-Photon Imaging—Glass windows for calcium imaging were implanted as described previously (Kato et al., 2015). In summary, mice were anaesthetized with isoflurane and injected with dexamethasone (2 mg/kg) intraperitoneally. A custom stainless steel head-bar was glued to the skull. Muscle overlying the right auditory cortex was removed and a craniotomy (~2 × 3 mm) was made, leaving the dura intact. Viruses (AAV2/9.syn.GCaMP6s.WPRE.SV40, AAV2/9.syn.FLEX.GCaMP6s.WPRE.SV40) were injected at 5–15 locations (250 μm deep from the pial surface, 20–30 nl/site). A glass window was placed over the craniotomy and secured with dental acrylic. Baytril (10 mg/kg) and buprenorphine (0.1 mg/kg) were injected before mice were returned to their home cages.

Preparation For In Vivo Electrophysiology—A head-bar was implanted as described for calcium imaging, and intrinsic signal imaging was performed through the intact skull. After mapping auditory cortex, the exposed skull was covered with silicone elastomer (KwikCast, WPI), and the mouse received buprenorphine (0.1 mg/kg) before returning to the home cage. 1–5 days later, mice were anaesthetized with isoflurane and the skull was exposed by removing the silicone cover. A small (< 0.3 mm diameter) craniotomy was made above A1 and a durotomy was made in some experiments. Special care was taken to reduce damage to the brain tissue during this surgery, since we observed abnormal activity from damaged tissue (see below). We found it critical to interrupt drilling every 1–2 s and cool the

skull with artificial cerebrospinal fluid (aCSF, in mM: 142 NaCl, 5 KCl, 10 glucose, 10 HEPES, 3.1 $CaCl_2$, 1.3 $MgCl_2$, pH 7.4) to prevent damage from overheating. Craniotomies were covered with aCSF and mice recovered from anesthesia for > 1.5 hr before whole-cell recording.

Sound Stimulus Presentation—Auditory stimuli were delivered via a free-field electrostatic speaker (ES1; Tucker-Davis Technologies). For intrinsic and calcium imaging, speakers were calibrated over a range of 2–40 kHz to give a flat response (±1 dB). For in vivo whole-cell recording, speakers were calibrated over a range of 4–60 kHz. Stimuli were delivered to the ear contralateral to imaging or recording. Auditory stimulus delivery was controlled by software (BControl; http://brodylab.org) running on MATLAB (MathWorks) communicating with a real-time system (RTLinux).

Intrinsic Signal Imaging—Intrinsic signal images were acquired using a tandem lens macroscope and 12 bit, CCD camera (CCD-1300QF, VDS Vosskühler). Mice were isoflurane-anaesthetized and injected with chlorprothixene (1.5 mg/kg, i.p.). Images of surface vasculature were acquired using green LED illumination (530 nm) and intrinsic signals were recorded (27 Hz) using red illumination (615 nm). Each trial consisted of 1 s baseline followed by a 1 s sound stimulus (75 dB pure tone with a frequency of 3, 10, or 30 kHz, 10–20 trials for each frequency) and 30 s inter-trial interval. Images of reflectance were acquired at 1024×1024 pixels (covering ~2.1×2.1 mm) and downsampled to 512×512 pixels by bilinear interpolation. Images during the response period (0.5–2 s from the sound onset) were averaged and divided by the average image during the baseline. Images were averaged across trials and Gaussian filtered.

In Vivo Two-Photon Calcium Imaging—Two-photon calcium imaging was performed ~three weeks after chronic window implantation to ensure an appropriate level of GCaMP6s expression. Intrinsic signal imaging was performed through chronic windows 1–3 days before calcium imaging to locate A1. On the day of calcium imaging, mice were head-fixed under the two-photon microscope in the awake state. GCaMP6s and tdTomato were excited at 920 nm (Mai Tai, Newport), and images (512×512 pixels covering ~500×500 μm) were acquired with a commercial microscope (B-scope, Thorlabs) running Scanimage software using a $16 \times$ objective (Nikon) at 28.4 Hz. Images were acquired from L2/3 (120–250 μm below the surface). Lateral motion was corrected by cross correlation-based image alignment.

In Vivo Whole-Cell Recording—Mice were acclimated to handling and head-fixation several days prior to recording. During recording, awake mice sat quietly (with occasional bouts of whisking and grooming) in a loosely fitted plastic tube within a sound attenuating enclosure. Whole-cell patch-clamp recordings were made with the blind technique. Most recorded cells were located in L2/3, based on the z axis readout of an MP-285 micromanipulator (Sutter; 200–300 μm from the pial surface; Figure S4). Voltage-clamp recordings were made with patch pipettes (3–4.5 MOhm) filled with internal solution composed of (in mM) 130 cesium gluconate, 10 HEPES, 5 TEA-Cl, 12 Na-phosphocreatine, 0.2 EGTA, 3 Mg-ATP, and 0.2 Na-GTP (7.2 pH; 310 mOsm). EPSCs and IPSCs were

recorded at −70 mV and +20 mV, near the reversal potentials for inhibition and excitation, respectively, set by our internal solution. Membrane potential values were not corrected for the ~15 mV liquid junction potential and series resistance was continuously monitored for stability (average 32.8 ± 2.1 MOhm, n = 38 cells). Current-clamp recordings were made with patch pipettes filled with internal solution composed of (in mM) 130 potassium gluconate, 5 NaCl, 10 HEPES, 12 Na-phosphocreatine, 0.2 EGTA, 3 Mg-ATP, and 0.2 Na-GTP (7.2 pH; 310 mOsm), except for input resistance measurements, in which the same internal solution as voltage-clamp recordings was used. Recordings were made with a MultiClamp 700A (Molecular Devices), digitized at 5–10 kHz (ITC-18, Instrutech), and acquired using AxographX (Axograph).

In awake mice, we observed a continuous barrage of spontaneous EPSCs and IPSCs (Figure 3A). Although previous studies reported low basal activity with intermittent spontaneous or sound-evoked bursts (Grienberger et al., 2012; Hromádka et al., 2008), we only observed bursting synaptic activity in damaged preparations (e.g., bleeding brain tissue, tissue overheated during drilling, or too many electrode penetrations). Since detection of network suppression was critically dependent on the presence of intact spontaneous activity, recordings were not performed in mice with surgical damage. Furthermore, experiments were terminated after 5–10 pipette penetrations when bursting activity appeared in recordings of EPSCs or field EPSPs.

In Vivo Optogenetic Inactivation Of Interneurons—For inactivation of specific interneuron subtypes, AAV2/9.EF1a.DIO.eNpHR3.0.EYFP.WPRE.hGH was injected into the right auditory cortex of newborn *SOM–Cre* or *PV–Cre* mice (postnatal day 1–2). Pups were anaesthetized by hypothermia and secured in a molded platform. Virus was injected at three locations along the rostral-caudal axis of the auditory cortex. At each site, injection was performed at three depths (600, 500, and 400 μm deep from the skin surface, 23 nl/depth). Six weeks after injections, in vivo voltage-clamp experiments were performed as described above, except that the entire skull over A1 was thinned to improve light penetration. A fiber-coupled LED (595 nm) was positioned 1–2 mm above the thinned skull. In interleaved trials, LED illumination was delivered that lasted from 200–300 ms before sound onset to 300 ms after sound offset. LED intensity was kept at the lowest effective intensity (~5–10 mW) to prevent aberrant sound-evoked cortical activity.

Slice Electrophysiology—For expressing ChR2 in genetically-identified interneurons, the following three methods were used: 1) AAV2/9.EF1a.DIO.hChR2(H134R).EYFP.WPRE.hGH or AAV2/9.CAGS.FLEX.hChR2(H134R).tdTomato.WPRE.SV40 was injected in the right A1 of adult *SOM-Cre* or *PV-Cre* mice, 2) AAV2/9.EF1a.DIO.hChR2(H134R).EYFP.WPRE.hGH was injected into the right auditory cortex of newborn *SOM–Cre* or *PV–Cre* mice, or 3) *SOM-Cre* or *PV-Cre* mice crossed with *Rosa-LSL-ChR2(H134R)-EYFP* mice. We did not observe differences between these conditions, and results were pooled. Slice electrophysiology experiments were performed in 6–12 week old mice, at least 10 days after virus injection. To prepare cortical slices that preserved A1 along its tonotopic axis, mice were anaesthetized with isoflurane and intrinsic

signal imaging was performed to map auditory areas. Small craniotomies (< 300 µm) were then made at the low- and high-frequency poles of the A1 tonotopic axis, and fluorescent beads (Lumifluor, 60–100 nl/site) were injected as landmarks. Mice were then anaesthetized with ketamine (200 mg/kg) and perfused with ice cold artificial cerebrospinal fluid (aCSF) containing (in mM) 83 NaCl, 2.5 KCl$_2$, 0.5 CaCl$_2$, 3.3 MgSO$_4$, 1 NaH$_2$PO$_4$, 26.2 NaHCO$_3$, 22 glucose, and 72 sucrose, equilibrated with 95%O$_2$ and 5%CO$_2$. The brain was removed and A1 cortical slices (500 µm thick) were cut perpendicular to the cortical surface at an angle such that the slice contained both bead-injection sites. Patch-clamp recordings were performed using an upright microscope and DIC optics. Recordings were made using a Multiclamp 700A amplifier, digitized at 20 kHz, and acquired and analyzed using AxographX software. Voltage-clamp recordings were made with patch pipettes (3–4.5 MOhm) filled with internal solution composed of (in mM) 130 cesium gluconate, 10 HEPES, 5 TEA-Cl, 12 Na-phosphocreatine, 0.2 EGTA, 3 Mg-ATP, and 0.2 Na-GTP (7.2 pH; 310 mOsm). Slices were superfused with aCSF containing (in mM): 119 NaCl, 5 KCl, 2.5 CaCl$_2$, 1.3 MgSO$_4$, 1 NaH$_2$PO$_4$, 26.2 NaHCO$_3$ and 22 glucose, equilibrated with 95% O$_2$ and 5% CO$_2$. All experiments were conducted in the presence of NBQX (10 µM, Tocris) and CGP55845 (10 µM, Tocris) at 30–32°C. IPSCs were recorded at 0 mV. Membrane potential values were not corrected for the liquid junction potential. Series resistance was routinely < 20 MOhm and continuously monitored. A collimated LED light source (470 nm, Thorlabs) was directed through a diaphragm and a 60 × microscope objective and restricted to a small spot (~60 µm diameter).

QUANTIFICATION AND STATISTICAL ANALYSIS

All data are presented as mean ± SEM. Statistically significant differences between conditions were determined using standard parametric or nonparametric tests in MATLAB. A two-tailed paired t test was used, unless otherwise stated. A nonparametric test (Wilcoxon signed rank test) was used to confirm statistical significances reported by t tests. All "n" values refer to the number of cells except when explicitly stated that the n is referring to the number of mice. Experiments were not performed blind. Sample sizes were not predetermined by statistical methods, but were based on those commonly used in the field.

Analysis Of Two-Photon Imaging Data—Regions of interest (ROIs) corresponding to visually identifiable cells were manually drawn, and pixels within each ROI were averaged to create a fluorescence time series $F_{cell\_measured}(t)$. To correct for neuropil contamination, ring-shaped background ROIs (starting at 2 pixels and ending at 8 pixels from the border of the ROI) were created around each cell ROI. From this background ROI, pixels that contained cell bodies or processes from surrounding cells were excluded. The remaining pixels were averaged to create a background fluorescence time series $F_{background}(t)$. The fluorescence signal of a cell body was estimated as $F(t) = F_{cell\_measured}(t) - 0.9 \times F_{background}(t)$. To ensure robust neuropil subtraction, only cell ROIs that were at least 3% brighter than the background ROIs were included. Sound-evoked responses were measured during one second tone presentations. Cells were judged as significantly excited (inhibited) if they fulfilled two criteria: 1) dF/F had to exceed a fixed threshold value consecutively for at least 0.5 s in more than half of trials. 2) dF/F averaged across trials had to exceed a fixed threshold value consecutively for at least 0.5 s. Threshold for excitation (1.9 × standard

deviation during baseline period) was determined by receiver operator characteristic (ROC) analysis to yield a 90% true positive rate in receptive field measurements. Since inhibitory responses tend to be small in amplitude, the threshold for inhibition was set as half that for excitation ($-0.95 \times$ standard deviation) to increase detection sensitivity. Two-photon imaging fields were aligned with the intrinsic signal imaging fields by comparing blood vessel patterns. Tonotopic positions of individual neurons in A1 were determined as the normalized distances such that '0' corresponds to the center of the 3 kHz-responding area, and '1' corresponds to the center of the 30 kHz-responding area of intrinsic signal imaging. If the center of the 10 kHz-responding area was not aligned to the 3 kHz- and 30 kHz centers, the field was warped so that the three landmarks form a straight line. BF was calculated as the frequency with the strongest response independent of tone intensity. For CF measurements, some cells had sound intensity thresholds lower than our lowest tested sound intensity (30 dB). CFs in these cells were estimated as the average of two measurements: 1) frequency with strongest response at lowest sound intensity, and 2) mean frequency of a fitted Gaussian for the responses across frequencies at lowest sound intensity (Issa et al., 2014).

Analysis Of Tuning Curve Shapes Of Individual Neurons—TRF shapes of individual imaged cells were classified into six categories by visual inspection of excitatory responses: V-shaped, V-unfilled, slanted, inverse-V, O-shaped, and random. TRF bandwidth of a neuron at each sound intensity was calculated as the average of the range of frequencies that evoked significant excitatory responses, and the range of frequencies in which a Gaussian fit to the peak amplitude-versus-frequency plot exceeds threshold value ($1.9 \times$ standard deviation during baseline period). Tuning broadness of each neuron was evaluated using three distinct measures: 1). Bandwidth$_{20}$, determined as the bandwidth of the TRF at 20 dB above threshold intensity (considering only cells with V-shaped, V-unfilled, or slanted TRFs). 2). Bandwidth at 70 dB SPL (considering only the cells with V-shaped, V-unfilled, or slanted TRFs). 3). Lifetime sparseness (Rolls and Tovee, 1995; Willmore and Tolhurst,

2001), which was calculated as $(1-\{[\sum_{j=1,N} r_j/N]^2/[\sum_{j=1,N} r_j^2/N]\})/(1-1/N)$, where r_j was the response peak amplitude of the cell to tone j, and N was the total number of tones. $1-Sp$ provides a measure of how much the response probability of a neuron was distributed equally among all tones (non-selective: $1-Sp=1$) versus attributable entirely to one tone (highly selective: $1-Sp=0$). Since calculation of $1-Sp$ does not rely on the TRF shape, it can also be used for quantifying the selectivity of inhibitory responses, which often do not have clear V-shape.

Analysis of In Vivo Electrophysiology—Data were analyzed using custom programs in MATLAB. Sound-evoked responses were measured using 100 ms tone presentations, except for current-clamp recordings and input resistance measurements, where tone durations were 200 ms and 500 ms, respectively. EPSC$_{ON}$ (IPSC$_{ON}$) was measured as negative (positive)-going current 20–40 ms after tone onset, and EPSC$_{NS}$ (IPSC$_{NS}$) was measured as positive (negative)-going current 50–175 ms after tone onset. Cells were judged as responsive to specific combinations of frequency and volume if they fulfilled two criteria: (1) the traces exceed a fixed threshold value consecutively for at least half the duration of detection window (i.e., 10 ms for EPSC$_{ON}$ and IPSC$_{ON}$, and 62.5 ms for EPSC$_{NS}$ and

IPSC$_{NS}$) in more than half of trials, and (2) the averaged trace across trials exceed a fixed threshold value consecutively for at least half the duration of detection window. Threshold for EPSC$_{ON}$ and IPSC$_{ON}$ was set as $0.5 \times$ standard deviation during baseline, and threshold for EPSC$_{NS}$ and IPSC$_{NS}$ was set as $0.3 \times$ standard deviation during baseline.

Data and Software Availability—The custom MATLAB code will be made available upon reasonable request.

Supplementary Material

Refer to Web version on PubMed Central for supplementary material.

Acknowledgments

References

Adesnik H, Scanziani M. Lateral competition for cortical space by layer-specific horizontal circuits. Nature. 2010; 464:1155–1160. [PubMed: 20414303]

Adesnik H, Bruns W, Taniguchi H, Huang ZJ, Scanziani M. A neural circuit for spatial summation in visual cortex. Nature. 2012; 490:226–231. [PubMed: 23060193]

Atallah BV, Bruns W, Carandini M, Scanziani M. Parvalbumin-expressing interneurons linearly transform cortical responses to visual stimuli. Neuron. 2012; 73:159–170. [PubMed: 22243754]

Calford MB, Semple MN. Monaural inhibition in cat auditory cortex. J Neurophysiol. 1995; 73:1876–1891. [PubMed: 7623087]

Carandini M, Ferster D. Membrane potential and firing rate in cat primary visual cortex. J Neurosci. 2000; 20:470–484. [PubMed: 10627623]

Constantinople CM, Bruno RM. Effects and mechanisms of wakefulness on local cortical networks. Neuron. 2011; 69:1061–1068. [PubMed: 21435553]

Gao L, Kostlan K, Wang Y, Wang X. Distinct subthreshold mechanisms underlying rate-coding principles in primate auditory cortex. Neuron. 2016; 91:905–919. [PubMed: 27478016]

Grienberger C, Adelsberger H, Stroh A, Milos RI, Garaschuk O, Schierloh A, Nelken I, Konnerth A. Sound-evoked network calcium transients in mouse auditory cortex in vivo. J Physiol. 2012; 590:899–918. [PubMed: 22106174]

Haider B, Krause MR, Duque A, Yu Y, Touryan J, Mazer JA, McCormick DA. Synaptic and network mechanisms of sparse and reliable visual cortical activity during nonclassical receptive field stimulation. Neuron. 2010; 65:107–121. [PubMed: 20152117]

Haider B, Häusser M, Carandini M. Inhibition dominates sensory responses in the awake cortex. Nature. 2013; 493:97–100. [PubMed: 23172139]

Hartline HK, Wagner HG, Ratliff F. Inhibition in the eye of Limulus. J Gen Physiol. 1956; 39:651–673. [PubMed: 13319654]

Hessler NA, Shirke AM, Malinow R. The probability of transmitter release at a mammalian central synapse. Nature. 1993; 366:569–572. [PubMed: 7902955]

Hromádka T, Deweese MR, Zador AM. Sparse representation of sounds in the unanesthetized auditory cortex. PLoS Biol. 2008; 6:e16. [PubMed: 18232737]

Isaacson JS, Scanziani M. How inhibition shapes cortical activity. Neuron. 2011; 72:231–243. [PubMed: 22017986]

Issa JB, Haeffele BD, Agarwal A, Bergles DE, Young ED, Yue DT. Multiscale optical Ca2+ imaging of tonal organization in mouse auditory cortex. Neuron. 2014; 83:944–959. [PubMed: 25088366]

Kato HK, Gillet SN, Isaacson JS. Flexible sensory representations in auditory cortex driven by behavioral relevance. Neuron. 2015; 88:1027–1039. [PubMed: 26586181]

Li LY, Li YT, Zhou M, Tao HW, Zhang LI. Intracortical multiplication of thalamocortical signals in mouse auditory cortex. Nat Neurosci. 2013; 16:1179–1181. [PubMed: 23933752]

Li LY, Ji XY, Liang F, Li YT, Xiao Z, Tao HW, Zhang LI. A feedforward inhibitory circuit mediates lateral refinement of sensory representation in upper layer 2/3 of mouse primary auditory cortex. J Neurosci. 2014; 34:13670–13683. [PubMed: 25297094]

Li LY, Xiong XR, Ibrahim LA, Yuan W, Tao HW, Zhang LI. Differential receptive field properties of parvalbumin and somatostatin inhibitory neurons in mouse auditory cortex. Cereb Cortex. 2015; 25:1782–1791. [PubMed: 24425250]

Lien AD, Scanziani M. Tuned thalamic excitation is amplified by visual cortical circuits. Nat Neurosci. 2013; 16:1315–1323. [PubMed: 23933748]

Litwin-Kumar A, Rosenbaum R, Doiron B. Inhibitory stabilization and visual coding in cortical circuits with multiple interneuron subtypes. J Neurophysiol. 2016; 115:1399–1409. [PubMed: 26740531]

Liu BH, Li YT, Ma WP, Pan CJ, Zhang LI, Tao HW. Broad inhibition sharpens orientation selectivity by expanding input dynamic range in mouse simple cells. Neuron. 2011; 71:542–554. [PubMed: 21835349]

McGinley MJ, David SV, McCormick DA. Cortical Membrane Potential Signature of Optimal States for Sensory Signal Detection. Neuron. 2015; 87:179–192. [PubMed: 26074005]

Mikaelian DO, Warfield D, Norris O. Genetic progressive hearing loss in the C57-b16 mouse. Relation of behavioral responses to chochlear anatomy. Acta Otolaryngol. 1974; 77:327–334. [PubMed: 4835632]

Moore AK, Wehr M. Parvalbumin-expressing inhibitory interneurons in auditory cortex are well-tuned for frequency. J Neurosci. 2013; 33:13713–13723. [PubMed: 23966693]

O'Connell MN, Falchier A, McGinnis T, Schroeder CE, Lakatos P. Dual mechanism of neuronal ensemble inhibition in primary auditory cortex. Neuron. 2011; 69:805–817. [PubMed: 21338888]

Ozeki H, Finn IM, Schaffer ES, Miller KD, Ferster D. Inhibitory stabilization of the cortical network underlies visual surround suppression. Neuron. 2009; 62:578–592. [PubMed: 19477158]

Pelleg-Toiba R, Wollberg Z. Tuning properties of auditory cortex cells in the awake squirrel monkey. Exp Brain Res. 1989; 74:353–364. [PubMed: 2924855]

Pfeffer CK, Xue M, He M, Huang ZJ, Scanziani M. Inhibition of inhibition in visual cortex: the logic of connections between molecularly distinct interneurons. Nat Neurosci. 2013; 16:1068–1076. [PubMed: 23817549]

Phillips DP, Cynader MS. Some neural mechanisms in the cat's auditory cortex underlying sensitivity to combined tone and wide-spectrum noise stimuli. Hear Res. 1985; 18:87–102. [PubMed: 4030512]

Poo C, Isaacson JS. Odor representations in olfactory cortex: "sparse" coding, global inhibition, and oscillations. Neuron. 2009; 62:850–861. [PubMed: 19555653]

Priebe NJ, Ferster D. Inhibition, spike threshold, and stimulus selectivity in primary visual cortex. Neuron. 2008; 57:482–497. [PubMed: 18304479]

Reinhold K, Lien AD, Scanziani M. Distinct recurrent versus afferent dynamics in cortical visual processing. Nat Neurosci. 2015; 18:1789–1797. [PubMed: 26502263]

Rolls ET, Tovee MJ. Sparseness of the neuronal representation of stimuli in the primate temporal visual cortex. J Neurophysiol. 1995; 73:713–726. [PubMed: 7760130]

Rubin DB, Van Hooser SD, Miller KD. The stabilized supralinear network: a unifying circuit motif underlying multi-input integration in sensory cortex. Neuron. 2015; 85:402–417. [PubMed: 25611511]

Rudy B, Fishell G, Lee S, Hjerling-Leffler J. Three groups of interneurons account for nearly 100% of neocortical GABAergic neurons. Dev Neurobiol. 2011; 71:45–61. [PubMed: 21154909]

Sadagopan S, Wang X. Contribution of inhibition to stimulus selectivity in primary auditory cortex of awake primates. J Neurosci. 2010; 30:7314–7325. [PubMed: 20505098]

Sato TK, Haider B, Häusser M, Carandini M. An excitatory basis for divisive normalization in visual cortex. Nat Neurosci. 2016; 19:568–570. [PubMed: 26878671]

Schneider DM, Nelson A, Mooney R. A synaptic and circuit basis for corollary discharge in the auditory cortex. Nature. 2014; 513:189–194. [PubMed: 25162524]

Scholl B, Gao X, Wehr M. Nonoverlapping sets of synapses drive on responses and off responses in auditory cortex. Neuron. 2010; 65:412–421. [PubMed: 20159453]

Shamma SA, Symmes D. Patterns of inhibition in auditory cortical cells in awake squirrel monkeys. Hear Res. 1985; 19:1–13. [PubMed: 4066511]

Steriade M, Timofeev I, Grenier F. Natural waking and sleep states: a view from inside neocortical neurons. J Neurophysiol. 2001; 85:1969–1985. [PubMed: 11353014]

Strichartz GR. The inhibition of sodium currents in myelinated nerve by quaternary derivatives of lidocaine. J Gen Physiol. 1973; 62:37–57. [PubMed: 4541340]

Sutter ML, Schreiner CE, McLean M, O'connor KN, Loftus WC. Organization of inhibitory frequency receptive fields in cat primary auditory cortex. J Neurophysiol. 1999; 82:2358–2371. [PubMed: 10561411]

Sutter ML, Loftus WC. Excitatory and inhibitory intensity tuning in auditory cortex: evidence for multiple inhibitory mechanisms. J Neurophysiol. 2003; 90:2629–2647. [PubMed: 12801894]

Talbot MJ, Sayer RJ. Intracellular QX-314 inhibits calcium currents in hippocampal CA1 pyramidal neurons. J Neurophysiol. 1996; 76:2120–2124. [PubMed: 8890325]

Tan AYY, Wehr M. Balanced tone-evoked synaptic excitation and inhibition in mouse auditory cortex. Neuroscience. 2009; 163:1302–1315. [PubMed: 19628023]

Tan AYY, Brown BD, Scholl B, Mohanty D, Priebe NJ. Orientation selectivity of synaptic input to neurons in mouse and cat primary visual cortex. J Neurosci. 2011; 31:12339–12350. [PubMed: 21865476]

Tremblay R, Lee S, Rudy B. GABAergic interneurons in the neocortex: from cellular properties to circuits. Neuron. 2016; 91:260–292. [PubMed: 27477017]

Tsodyks MV, Skaggs WE, Sejnowski TJ, McNaughton BL. Paradoxical effects of external modulation of inhibitory interneurons. J Neurosci. 1997; 17:4382–4388. [PubMed: 9151754]

Urban-Ciecko J, Fanselow EE, Barth AL. Neocortical somatostatin neurons reversibly silence excitatory transmission via GABAb receptors. Curr Biol. 2015; 25:722–731. [PubMed: 25728691]

Wehr M, Zador AM. Balanced inhibition underlies tuning and sharpens spike timing in auditory cortex. Nature. 2003; 426:442–446. [PubMed: 14647382]

Wehr M, Zador AM. Synaptic mechanisms of forward suppression in rat auditory cortex. Neuron. 2005; 47:437–445. [PubMed: 16055066]

Willmore B, Tolhurst DJ. Characterizing the sparseness of neural codes. Network. 2001; 12:255–270. [PubMed: 11563529]

Wu GK, Arbuckle R, Liu BH, Tao HW, Zhang LI. Lateral sharpening of cortical frequency tuning by approximately balanced inhibition. Neuron. 2008; 58:132–143. [PubMed: 18400169]

Xu X, Roby KD, Callaway EM. Immunochemical characterization of inhibitory mouse cortical neurons: three chemically distinct classes of inhibitory cells. J Comp Neurol. 2010; 518:389–404. [PubMed: 19950390]

Zhang LI, Tan AY, Schreiner CE, Merzenich MM. Topography and synaptic shaping of direction selectivity in primary auditory cortex. Nature. 2003; 424:201–205. [PubMed: 12853959]

Zhang S, Xu M, Kamigaki T, Hoang Do JP, Chang WC, Jenvay S, Miyamichi K, Luo L, Dan Y. Selective attention. Long-range and local circuits for top-down modulation of visual cortex processing. Science. 2014; 345:660–665. [PubMed: 25104383]

Zhou M, Liang F, Xiong XR, Li L, Li H, Xiao Z, Tao HW, Zhang LI. Scaling down of balanced excitation and inhibition by active behavioral states in auditory cortex. Nat Neurosci. 2014; 17:841–850. [PubMed: 24747575]

Author Manuscript

Author Manuscript

Author Manuscript

Author Manuscript

Highlights

- Frequency tuning in auditory cortex of mice is shaped by lateral inhibition

- Lateral inhibition is due to the suppression of recurrent excitation

- Somatostatin-expressing interneurons trigger network suppression

- Auditory cortex operates as an inhibition-stabilized network (ISN)
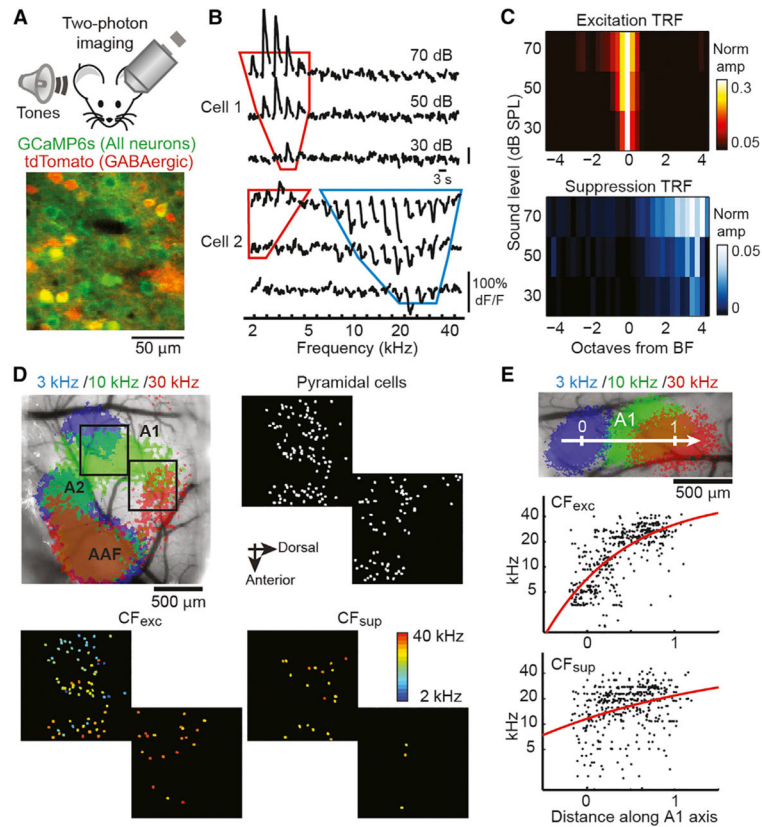
**Figure 1. Lateral Inhibition in Auditory Cortex of Awake Mice**

(A) Top, imaging schematic. Bottom, *in vivo* image of GCaMP6s (green)- and tdTomato (red)-expressing cells in L2/3 of A1.

(B) Frequency tuning of two representative L2/3 pyramidal cells measured with two-photon calcium imaging. Traces are average responses (five trials) for each frequency-intensity pair. Red and blue lines outline excitatory and suppressive TRFs, respectively.

(C) Lateral inhibition is prominent at high frequencies. Summary plot of excitatory and suppressive TRFs averaged across all cells with excitatory responses (n = 749 cells, 8 mice). Responses are centered at the best frequency (BF) for excitation and normalized to the maximum response of each neuron.

(D) Cellular level tonotopic organization of A1. Top left, intrinsic signal imaging of responses to pure tones (3, 10, and 30 kHz) superimposed on image of cortical vasculature. A1, primary auditory cortex; A2, secondary auditory cortex; AAF, anterior auditory field. Black squares, locations of two-photon imaging. Top right, map of imaged pyramidal cells. Bottom, activity maps showing the characteristic frequency for excitation (CF_{exc}) and suppression (CF_{sup}) of the imaged cells.

(E) Mismatch in the frequency tuning of excitation and suppression along the A1 tonotopic axis. Top, image of intrinsic signal showing reference points used for normalizing distance along the A1 tonotopic axis across animals. Middle, CF_{exc} of individual cells coheres to the macroscopic tonotopy of A1. Bottom, mapping CF_{sup} shows that tone-evoked suppression is less sharply aligned to A1 tonotopy and high frequencies are uniformly overrepresented.
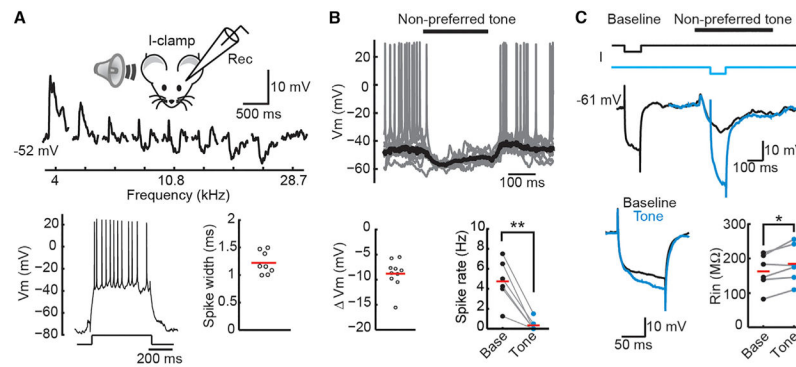
Figure 2. Membrane Hyperpolarization and Unconventional Increase in Cell Input Resistance Underlie Lateral Inhibition

(A) Top, recording schematic and membrane potential responses of a representative cell to tones (nine frequencies, 70 dB, 200 ms) show shift from depolarization to hyperpolarization as frequency increases. Spikes digitally removed. Bottom left, representative cell with regular spiking response in current-clamp (400 pA current step). Bottom right, summary data for spike half-maximum width. The distribution shows a single cluster with values typical for pyramidal cells (1.22 ± 0.07 ms, n = 8 cells). Rec, recording pipette. Red line, mean.

(B) Top, hyperpolarization and spike suppression in response to non-preferred tone (30 kHz) in a representative cell. Gray traces, five consecutive trials near firing threshold. Black trace, mean membrane potential across trials after removing spikes. Bottom left, summary data of peak hyperpolarization evoked by non-preferred tones (-8.8 ± 0.9 mV, n = 10 cells, p = 4×10^{-6}). Bottom right, summary data showing the suppression of spikes during non-preferred tones (95% $\pm$ 3% suppression, n = 6 cells, **p = 2×10^{-3}).

(C) Cell input resistance increases during inhibition at non-preferred frequencies. Top, membrane response to current steps (I, -100 pA) in a representative cell before (Baseline) and during a non-preferred tone (bar, 30 kHz). Traces are averages of interleaved trials in which the current step was before (black) or during (blue) the tone. Bottom left, membrane response to current injection during the tone overlaid on the baseline response indicates an increase in membrane resistance. The membrane response to current steps during the tone (blue trace) was obtained by subtracting tone-evoked responses without current steps. Bottom right, summary of cell input resistance (Rin) change during non-preferred tones (n = 6 cells, 4 mice). Red bars, mean. *p = 0.0297. Results are mean $\pm$ SEM.
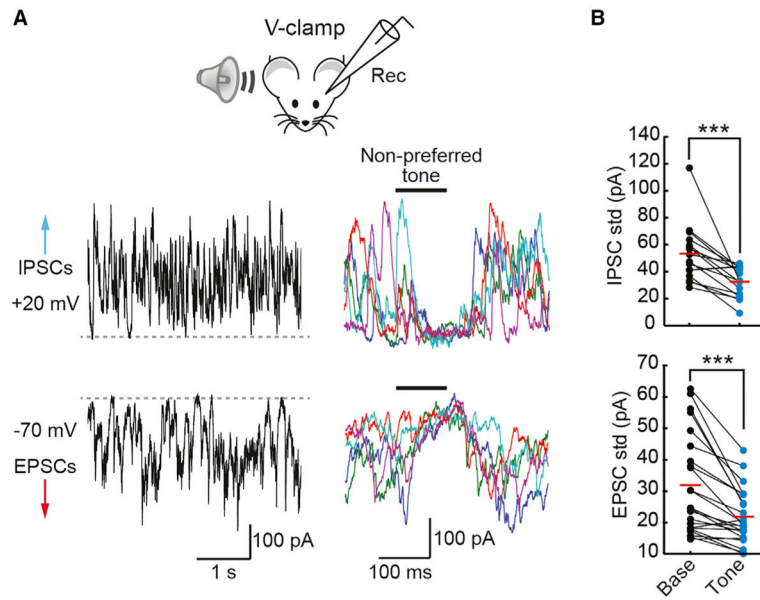
Figure 3. Non-preferred Stimuli Suppress Spontaneous Synaptic Excitation and Inhibition during Lateral Inhibition

(A) Top, recording schematic. Bottom left, voltage-clamp recordings show continuous, high-frequency barrages of spontaneous IPSCs (top) and EPSCs (bottom). Dashed lines indicate putative "baseline" current levels when spontaneous activity is low. Bottom right, traces from the same cell on a faster timescale show that a non-preferred tone suppresses both spontaneous EPSCs and IPSCs. Five consecutive trials are displayed in different colors. Black bars, tone.

(B) Summary of the reduction of spontaneous synaptic activity determined from membrane current standard deviation (std) before and during non-preferred tones. Standard deviations of IPSCs (top) and EPSCs (bottom) are reduced during tones (IPSC, 36% ± 6%, n = 16 cells, ***p = 8×10^{-4}; EPSC, 26% ± 4%, n = 23 cells, ***p = 6×10^{-5}). Results are mean ± SEM.
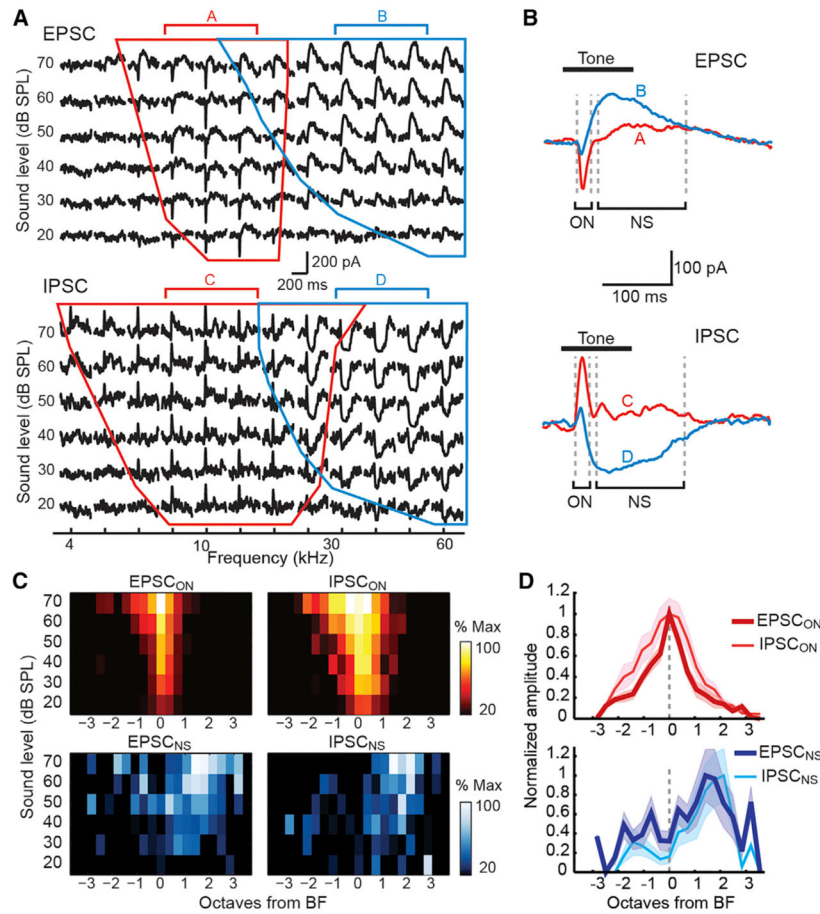
Figure 4. Preferred Frequencies Evoke Fast, Onset-Locked EPSCs and IPSCs, while Non-preferred Frequencies Elicit Slow Network Suppression of Spontaneous Synaptic Activity

(A) Frequency tuning of tone-evoked EPSCs and IPSCs in one cell. Traces are average responses for each frequency-intensity pair. Red lines outline TRF region with fast, onset-locked components ($EPSC_{ON}$ and $IPSC_{ON}$), blue lines indicate region with slow network suppression ($EPSC_{NS}$ and $IPSC_{NS}$).

(B) EPSC and IPSC from (A) averaged across frequencies with onset-locked responses (A and C, red) and network suppression (B and D, blue). Gray dotted lines mark windows for measuring individual components.

(C) TRFs for $EPSC_{ON}$, $IPSC_{ON}$, $EPSC_{NS}$, and $IPSC_{NS}$ averaged across cells (n = 23 cells, 17 mice). Responses are centered at $EPSC_{ON}$ best frequency (BF) for each cell.

(D) Summary of the frequency tuning of the four components at 50–70 dB. Response amplitudes are normalized to their individual peaks. Dark line, mean; shading, SEM.
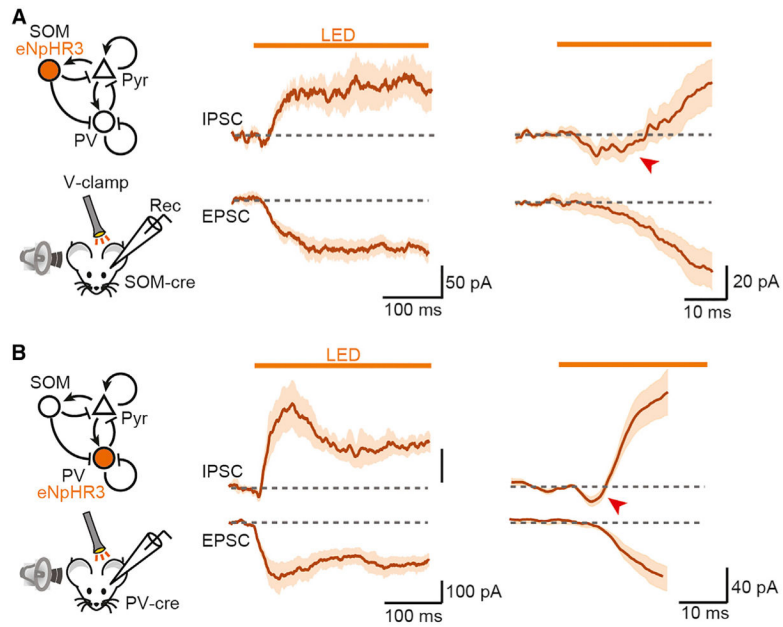
Figure 5. Suppression of Interneurons Causes a Paradoxical Increase in Pyramidal Cell-Inhibitory Synaptic Current

(A) Left, schematic of optogenetic inactivation of SOM cells during *in vivo* voltage-clamp recording. Circuit based on Pfeffer et al., 2013. Middle, photoinactivation of SOM cells increases spontaneous EPSCs and IPSCs. Traces show average responses across experiments (n = 12 cells, 8 mice). Dark trace, mean across cells. Shading, SEM. Orange bars, LED. Right, blow-up of the traces at LED onset shows the transient reduction in inhibition (red arrowhead) that precedes the paradoxical increase in IPSC.

(B) PV cell inactivation experiments. EPSCs and IPSCs as shown in A (n = 9 cells, 5 mice).
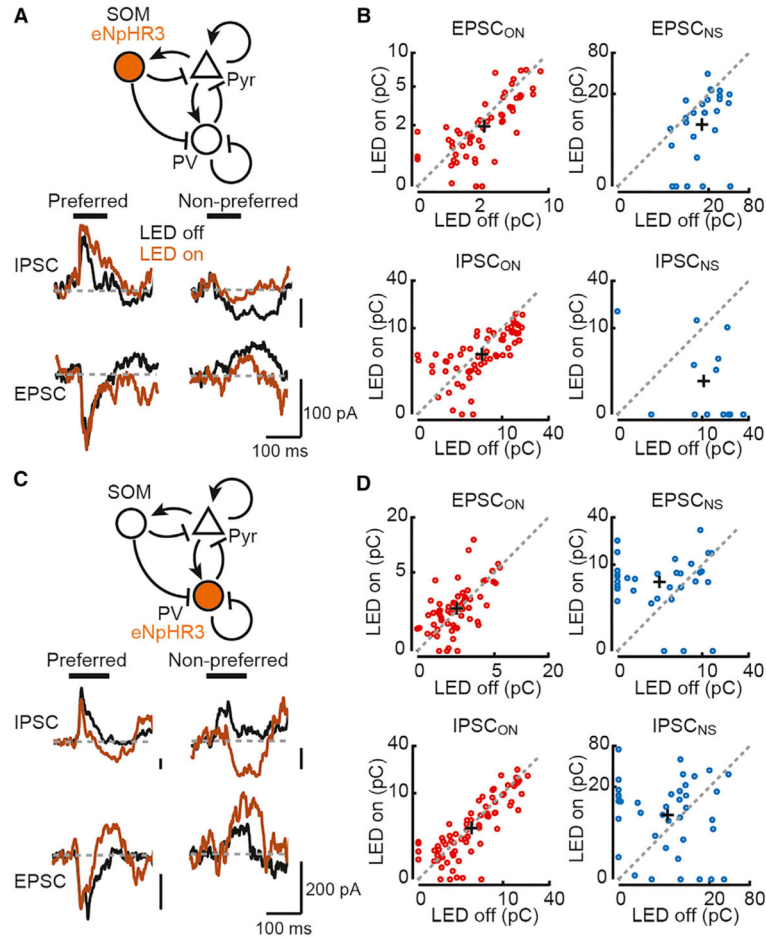
Figure 6. SOM Cells Trigger Network Suppression Underlying Lateral Inhibition

(A) SOM cell inactivation reduces tone-evoked network suppression. Top, schematic. Bottom, tone-evoked EPSCs and IPSCs of a representative cell with (brown) and without (black) SOM cell photoinactivation. Responses during photoinactivation were evoked 300 ms after LED onset and baselined to the 50 ms period before tone onset. Preferred and non-preferred tones (black bars, 70 dB) are 8.4 and 36.7 kHz, respectively.

(B) Average magnitude of synaptic currents ($EPSC_{ON}$, $IPSC_{ON}$, $EPSC_{NS}$, and $IPSC_{NS}$) during LED on and LED off trials for responsive cell-tone pairs (n = 7 cells, 5 mice) plotted on log-modulus scale. Dashed lines, unity. Black crosses, average.

(C) PV cell inactivation enhances network suppression. Top, schematic. Bottom, tone-evoked EPSCs and IPSCs of a representative cell with (brown) and without (black) PV cell photoinactivation. Preferred and non-preferred tones (black bars, 70 dB) are 13.7 and 36.7 kHz, respectively.

(D) Average magnitude of response components during LED on and LED off trials for responsive cell-tone pairs (n = 8 cells, 5 mice).
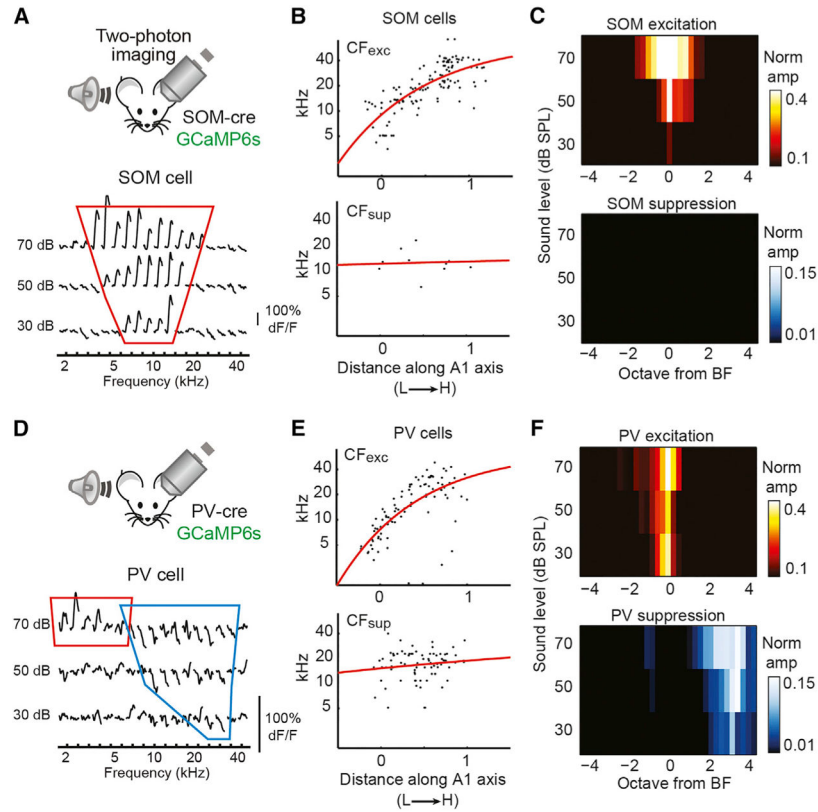
Figure 7. SOM Cells Receive Broadly Tuned Excitation

(A) Top, approach. Bottom, frequency tuning of representative SOM cell. Red, outline of excitatory TRF.

(B) Top, map of characteristic frequency for excitation (n = 142 cells, 5 mice) shows that SOM cells are tuned and aligned to the A1 tonotopic axis. Bottom, map of CF for suppression. Red lines, single exponential fit to data.

(C) TRF for SOM cells reveal broadly tuned excitation and no lateral inhibition. Data are centered at the best frequency for excitation and normalized to the maximum response of each neuron.

(D) Top, approach. Bottom, frequency tuning of representative PV cell with excitatory (red) and suppressive (blue) TRF.

(E) Maps of characteristic frequencies for excitation and suppression of PV cells (n = 101 cells, 6 mice) are similar to pyramidal cells.

(F) TRFs for PV cells reveal excitation and lateral inhibition similar to pyramidal cells.
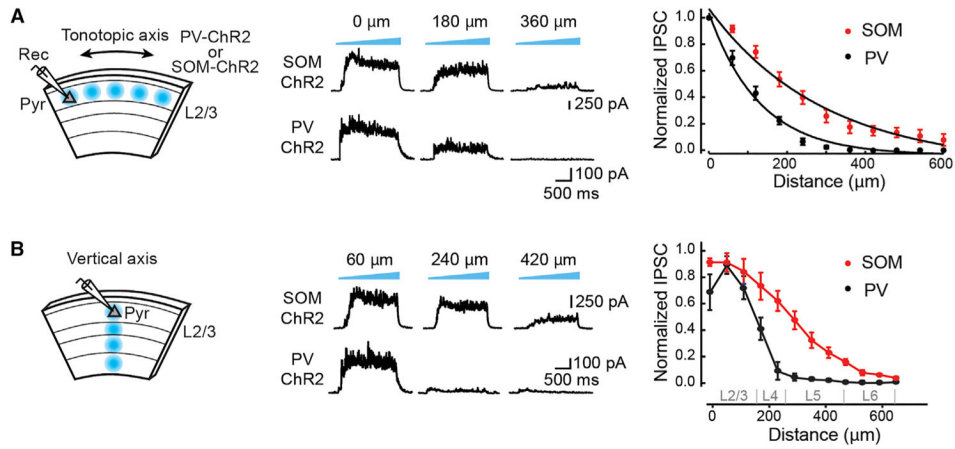
Figure 8. SOM Cells Inhibit Wide Regions of Cortical Space

(A) Left, schematic of brain slice experiment using focal illumination along the A1 tonotopic axis to test input to L2/3 pyramidal cells from ChR2-expressing SOM and PV cells. Middle, IPSCs evoked by light ramps (blue) at increasing horizontal distances from the recorded cell body (0 μm) in a slice expressing ChR2 in SOM cells (upper traces) or PV cells (bottom traces). Right, summary showing that SOM cells (red, n = 12 cells, 5 mice) provide inhibition over a greater horizontal distance than PV cells (black, n = 12 cells, 6 mice). Data (mean ± SEM) are fit with a single exponential. Normalized IPSC at 300 μm: PV = 0.03 ± 0.01, SOM= 0.26 ± 0.05, p = < 0.001.

(B) Same as in A but focal illumination is applied along a cortical column. Distance is plotted from cell body in L2/3 (0 μm) toward the white matter. Normalized IPSC at 300 μm: PV = 0.04 ± 0.03, SOM = 0.47 ± 0.07, p = < 0.001.